

---

5-1-2022

## The Dense Gas Mass Fraction and the Relationship to Star Formation in M51

Mark Heyer

*University of Massachusetts Amherst*

Benjamin Gregg

*University of Massachusetts Amherst*

Daniela Calzetti

*University of Massachusetts Amherst*

Bruce G. Elmegreen

*IBM Thomas J. Watson Research Center*

Robert Kennicutt

*The University of Arizona*

*See next page for additional authors*

Follow this and additional works at: [https://scholarworks.smith.edu/ast\\_facpubs](https://scholarworks.smith.edu/ast_facpubs)



Part of the [Astrophysics and Astronomy Commons](#)

---

### Recommended Citation

Heyer, Mark; Gregg, Benjamin; Calzetti, Daniela; Elmegreen, Bruce G.; Kennicutt, Robert; Adamo, Angela; Evans, Aaron S.; Grasha, Kathryn; Lowenthal, James D.; Narayanan, Gopal; Rosa-Gonzalez, Daniel; Schloerb, F. P.; Souccar, Kamal; Tang, Yuping; Teuben, Peter; Vega, Olga; Wall, William F.; and Yun, Min S., "The Dense Gas Mass Fraction and the Relationship to Star Formation in M51" (2022). Astronomy: Faculty Publications, Smith College, Northampton, MA.  
[https://scholarworks.smith.edu/ast\\_facpubs/84](https://scholarworks.smith.edu/ast_facpubs/84)

This Article has been accepted for inclusion in Astronomy: Faculty Publications by an authorized administrator of Smith ScholarWorks. For more information, please contact [scholarworks@smith.edu](mailto:scholarworks@smith.edu)

---

## Authors

Mark Heyer, Benjamin Gregg, Daniela Calzetti, Bruce G. Elmegreen, Robert Kennicutt, Angela Adamo, Aaron S. Evans, Kathryn Grasha, James D. Lowenthal, Gopal Narayanan, Daniel Rosa-Gonzalez, F. P. Schloerb, Kamal Souccar, Yuping Tang, Peter Teuben, Olga Vega, William F. Wall, and Min S. Yun



# The Dense Gas Mass Fraction and the Relationship to Star Formation in M51

Mark Heyer<sup>1</sup>, Benjamin Gregg<sup>1</sup>, Daniela Calzetti<sup>1</sup>, Bruce G. Elmegreen<sup>2</sup>, Robert Kennicutt<sup>3,4</sup>, Angela Adamo<sup>5</sup>, Aaron S. Evans<sup>6,7</sup>, Kathryn Grasha<sup>8,9</sup>, James D. Lowenthal<sup>10</sup>, Gopal Narayanan<sup>1</sup>, Daniel Rosa-Gonzalez<sup>11</sup>, F. P. Schloerb<sup>1</sup>, Kamal Souccar<sup>1</sup>, Yuping Tang<sup>12</sup>, Peter Teuben<sup>13</sup>, Olga Vega<sup>11</sup>, William F. Wall<sup>11</sup>, and Min S. Yun<sup>1</sup>

<sup>1</sup>Astronomy Department, University of Massachusetts, Amherst, MA, 01003, USA; [heyer@astro.umass.edu](mailto:heyer@astro.umass.edu)

<sup>2</sup>IBM Research Division, T. J. Watson Research Center, 1101 Kitchawan Road, Yorktown Heights, NY 10598, USA

<sup>3</sup>Steward Observatory, University of Arizona, Tucson, AZ 85721-0065, USA

<sup>4</sup>George P. and Cynthia W. Mitchell Institute for Fundamental Physics & Astronomy, Texas A&M University, College Station, TX, 77843-4242, USA

<sup>5</sup>The Oskar Klein Centre, Department of Astronomy, Stockholm University, AlbaNova, SE-10691 Stockholm, Sweden

<sup>6</sup>Astronomy Department, University of Virginia, 530 McCormick Road, Charlottesville, VA, 22904, USA

<sup>7</sup>National Radio Astronomy Observatory, 520 Edgemont Road, Charlottesville, VA, 22903, USA

<sup>8</sup>Research School of Astronomy and Astrophysics, Australian National University, Canberra ACT 2611, Australia

<sup>9</sup>ARC Centre of Excellence for All Sky Astrophysics in 3 Dimensions (ASTRO 3D), Australia

<sup>10</sup>Department of Astronomy, Smith College, Northampton, MA 01063, USA

<sup>11</sup>Instituto Nacional de Astrofísica, Óptica y Electrónica, Tonantzintla, 72840, Puebla, Mexico

<sup>12</sup>Chinese Academy of Sciences South America Center for Astronomy, National Astronomical Observatories, CAS, Beijing, 100012, People's Republic of China

<sup>13</sup>Department of Astronomy, University of Maryland, College Park, MD, 20742, USA

Received 2022 January 10; revised 2022 March 28; accepted 2022 April 14; published 2022 May 17

## Abstract

Observations of  $^{12}\text{CO } J=1-0$  and  $\text{HCN } J=1-0$  emission from NGC 5194 (M51) made with the 50 m Large Millimeter Telescope and the SEQUOIA focal plane array are presented. Using the HCN-to-CO ratio, we examine the dense gas mass fraction over a range of environmental conditions within the galaxy. Within the disk, the dense gas mass fraction varies along the spiral arms but the average value over all spiral arms is comparable to the mean value of interarm regions. We suggest that the near-constant dense gas mass fraction throughout the disk arises from a population of density-stratified, self-gravitating molecular clouds and the required density threshold to detect each spectral line. The measured dense gas fraction significantly increases in the central bulge in response to the effective pressure,  $P_e$ , from the weight of the stellar and gas components. This pressure modifies the dynamical state of the molecular cloud population and, possibly, the HCN-emitting regions in the central bulge from self-gravitating to diffuse configurations in which  $P_e$  is greater than the gravitational energy density of individual clouds. Diffuse molecular clouds comprise a significant fraction of the molecular gas mass in the central bulge, which may account for the measured sublinear relationships between the surface densities of the star formation rate and molecular and dense gas.

*Unified Astronomy Thesaurus concepts:* [Interstellar clouds \(834\)](#); [Dense interstellar clouds \(371\)](#); [Galaxy environments \(2029\)](#); [Star forming regions \(1565\)](#)

## 1. Introduction

The birth of a star is marked by the ignition of thermonuclear burning in the central core of a protostellar object. This remarkable event is the endpoint of a sequence of processes that redistribute neutral interstellar gas into increasingly higher-density configurations. Large, massive molecular clouds emerge from the neutral atomic component of the interstellar medium (ISM). These molecular clouds fragment into higher-density clumps and filaments (André et al. 2014). Within the clumps and filaments, high-density prestellar cores develop that ultimately collapse under their own self-gravity to initiate the protostellar stage from which a star is ultimately produced (Beuther et al. 2007; Gieser et al. 2021). In each step, only a small fraction of the gas mass is converted into the next, higher-density stage. The low yields for these transitions contribute to the measured inefficiency of star formation in which only  $\sim 1\%$  of gas mass is converted into stars over a freefall timescale as evaluated from whole galaxies to molecular clouds (Krumholz et al. 2012; Pokhrel et al. 2021).

Observations of resolved molecular clouds in the solar neighborhood of the Milky Way have long demonstrated the spatial link between recent star formation and localized pockets of gas with volume densities greater than  $10^4 \text{ cm}^{-3}$  (Myers & Benson 1983; Bergin & Tafalla 2007; Wu et al. 2010). Gao & Solomon (2004a) extended this connection to galaxies by identifying a relationship between the infrared luminosity, a measure of the star formation rate, SFR, and the luminosity of  $\text{HCN } J=1-0$  emission, a proxy for dense, molecular gas mass. Since that study, follow-up investigations with increasingly higher angular resolution, coverage, and sensitivity toward nearby galaxies have extended the relationship over 10 dex in HCN luminosity (Jiménez-Donaire et al. 2019).

Gas overdensities within molecular clouds are readily generated by the effects of gravity, the slow diffusion of the interstellar magnetic field, and supersonic super-Alfvénic motions within a cloud. However, molecular clouds are not isolated objects but are part of the larger ecosystem of a galaxy. The local galactic environment can modulate the properties of molecular clouds (Meidt 2016). Such environmental factors include the midplane pressure from the weight of stars, gas, and dark matter; the action of spiral density waves in disk galaxies that compress and redirect gas flows entering the spiral gravitational potential; and radiative and mechanical feedback

from massive stars that inject momentum and energy into cloud volumes that drive and sustain turbulent flows.

The galaxy NGC 5194 (M51a) is an appropriate target to study the role of the local environment in the development of overdense regions in molecular clouds. M51a (hereafter M51) exhibits a central bulge and prominent spiral structure within a molecular gas-rich disk that is actively forming new stars (Bigiel et al. 2016). The tidal interaction of M51a with its companion, M51b (NGC 5195), is likely responsible for exciting the strong spiral density waves (Dobbs et al. 2010). Its nearly face-on view provides a clear perspective of the spiral arms and interarm regions.

In this contribution, we investigate the spatial distribution of the dense gas fraction derived from the HCN-to-CO ratio of luminosities within M51 using new data from the 50 m Large Millimeter Telescope. We investigate the role of spiral structure in modulating the formation and development of dense clumps and filaments over the ensemble of molecular clouds within our telescope beam and its impact on the rate and efficiency of star formation. In Section 2, we describe the data presented in this study. Images of  $^{12}\text{CO}$  and HCN  $J=1-0$  emission are presented in Section 3, along with descriptions of how the star formation rates and stellar-mass surface densities are derived. Variations of the dense gas mass fraction with environment are examined in Section 4. The scaling relationships between star formation and both molecular and dense gas are analyzed in Section 5. In Section 6, we discuss our results.

## 2. Data

### 2.1. Molecular Line Emission

Observations of  $^{12}\text{CO}$   $J=1-0$  and HCN  $J=1-0$  emission from M51 were obtained with the 50 m Large Millimeter Telescope (LMT) Alfonso Serrano between 2020 January and March, using the 16 element focal plane array receiver SEQUOIA. The half-power beamwidths (HPBW) of the telescope at the line rest frequencies for CO (115.2712018 GHz) and HCN (88.630416 GHz) are  $12''$  and  $16''$ , respectively. The Wide-band Array Roach Enabled Spectrometer (WARES) was used to process the spectral information using the configuration with 800 MHz bandwidth and 391 kHz per spectral channel, which provides a velocity resolution of  $1.1 \text{ km s}^{-1}$  for CO and  $1.3 \text{ km s}^{-1}$  for HCN.

For  $^{12}\text{CO}$ , 10 maps covering the same  $10' \times 10'$  area were observed using On-the-Fly (OTF) mapping with all scanning along the R.A. axis. HCN imaging comprised multiple OTF maps covering three  $7' \times 4'$  overlapping areas centered on the nucleus of M51,  $2'$  north of the nucleus, and  $2'$  south of the nucleus. Data were calibrated by a chopper wheel that allowed switching between the sky and an ambient temperature load. The chopper wheel method introduces a fractional uncertainty of  $\sim 10\%$  to the measured antenna temperatures (Narayanan et al. 2008). Routine pointing and focus measurements were made to ensure positional accuracy and optimal gain.

All data were processed with the LMT spectral line software package, which included zero-order baseline subtraction and the coadding of multiple maps into a final spectral line data cube at the native angular and spectral resolutions. To directly compare the  $^{12}\text{CO}$  and HCN intensities, we also processed the  $^{12}\text{CO}$  data to the HCN resolution  $\lambda/D=14''$  and  $\lambda/2D=7''$  sampling, where  $D$  is the 50 m diameter of the LMT antenna. At a distance of  $8.58 \pm 0.10 \text{ Mpc}$  (McQuinn et al. 2016), this

resolution corresponds to a spatial size of 582 pc. Both CO and HCN data cubes were spectrally smoothed and resampled to  $5 \text{ km s}^{-1}$  resolution. A main-beam efficiency of 0.65 is applied to convert the data from the  $T_A^*$  temperature scale to main-beam temperatures. The median rms sensitivities in main-beam temperature units at  $5 \text{ km s}^{-1}$  spectral resolution are 28 mK for  $^{12}\text{CO}$  and 8 mK for HCN.

### 2.2. Ancillary Data

Our analysis requires several ancillary data sets. To measure the unobscured star formation rates, we use far-ultraviolet (FUV) data taken from the GALEX Ultraviolet Atlas of Nearby Galaxies (Gil de Paz et al. 2007). The obscured star formation rate is derived from the Spitzer MIPS  $24 \mu\text{m}$  data from the Spitzer Infrared Nearby Galaxies Survey (SINGS) (Kennicutt & Armus 2003). Models of the galactic structure are derived from the  $3.6 \mu\text{m}$  image from SINGS. The mass of the stellar component of M51 is calculated using the  $H$ -band image from 2MASS (Jarrett et al. 2003), supplemented by  $g$ - and  $i$ -band images from the Sloan Digital Sky Survey (SDSS-III) (Aihara et al. 2011) and produced by Brown et al. (2014). All ancillary data sets were obtained from the NASA/IPAC Extragalactic Database (NED).

## 3. Results

### 3.1. Molecular Line Images

Images of velocity-integrated CO  $J=1-0$  emission and HCN  $J=1-0$  emission are displayed in Figure 1. These images are created by masking the spectral channels where CO is detected for each spectrum in the coadded map in order to limit contributions of noise that can occur when integrating over a fixed, wide velocity interval of a rotating galaxy. This masking is achieved by the following steps described by Dame (2011). First, the CO data are smoothed along the angular axes using a Gaussian kernel with an HPBW of 5 pixels ( $35''$ ) and along the spectral axis using a boxcar kernel with a width of three spectral channels ( $15 \text{ km s}^{-1}$ ) while keeping the angular and spectral sampling of  $7''$  and  $5 \text{ km s}^{-1}$ . For a given spectrum in the smoothed data cube, any grouping of three or more consecutive channels with brightness temperatures greater than  $3.75\sigma$  is flagged as active voxels and assigned a value of 1 in the mask data cube,  $M(x, y, \nu)$ . All other channels are assigned a value of zero. This signal-to-noise threshold is a result of many trials with varying signal-to-noise ratios to maximize the number of active pixels while minimizing false detections. The integrated intensity image,  $W$ , is calculated from the data cube,  $T_{\text{mb}}(x, y, \nu)$  from the expression

$$W(x, y) = \Delta\nu \sum_k T_{\text{mb}}(x, y, \nu_k) M(x, y, \nu_k), \quad (1)$$

where the sum is over all spectral channels and  $\Delta\nu$  is the channel width of  $5 \text{ km s}^{-1}$ . The statistical error of this integrated intensity is  $\sigma(x, y) \Delta\nu (N_c(x, y))^{1/2}$ , where  $\sigma(x, y)$  is the rms of channels outside the velocity range  $360\text{--}800 \text{ km s}^{-1}$  of the unsmoothed data cube and  $N_c(x, y)$  is the number of active channels for position  $x, y$ .

The left panel in Figure 1 shows widespread detection of  $^{12}\text{CO}$  emission over the projected area of M51. The brightest emission traces the bulge and inner spiral features identified in previous studies with comparable resolution (Koda et al. 2011; Pety et al. 2013). Signal is also detected within the interarm

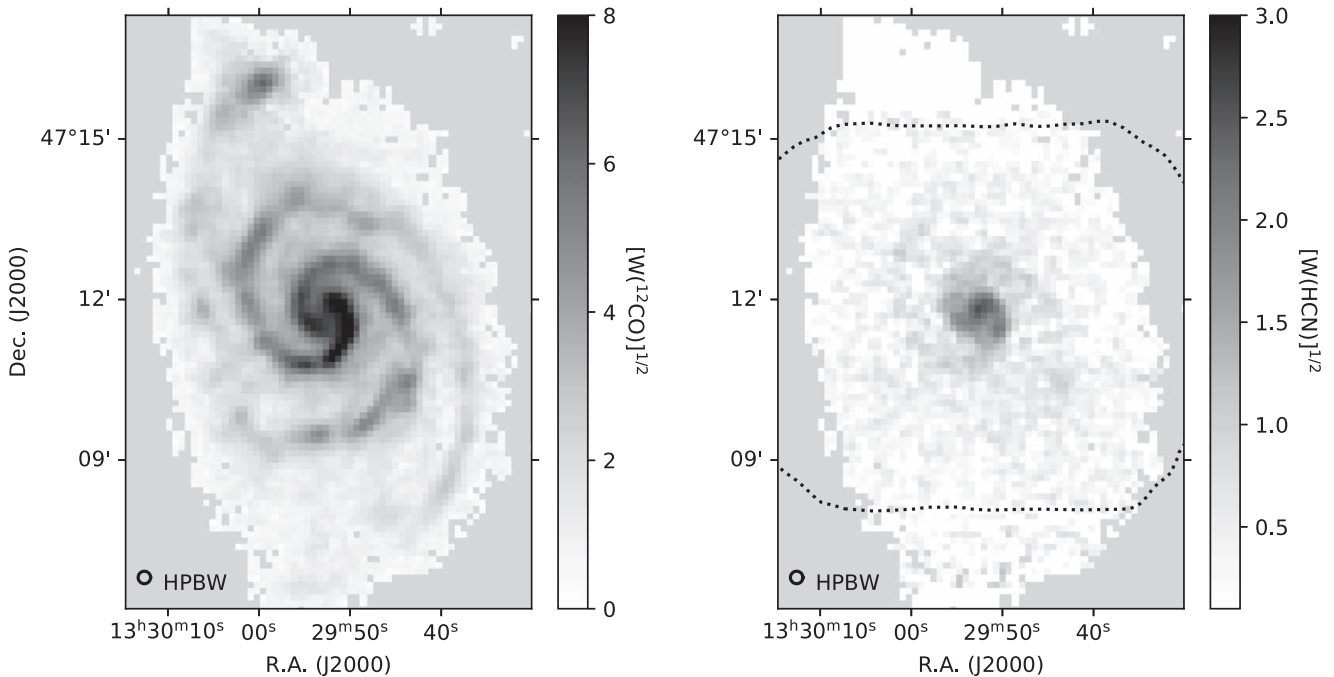


**Figure 1.** (Left) Masked image of  $(W(\text{CO}))^{1/2}$ . The square root of integrated intensity values is displayed in order to enhance the low-surface-brightness features. The median uncertainty of  $W(\text{CO})$  is  $0.44 \text{ K km s}^{-1}$ . (Right) Masked image of  $(W(\text{HCN}))^{1/2}$  using the  $^{12}\text{CO}$ -defined mask. The median uncertainty of  $W(\text{HCN})$  is  $0.10 \text{ K km s}^{-1}$ . The dotted contour marks the 90th percentile of HCN rms values.

regions—even within the large, interarm area in the south. Integrating the CO emission over all pixels, we derive a CO luminosity of  $(2.167 \pm 0.003) \times 10^9 \text{ K km s}^{-1} \text{ pc}^2$ , assuming a distance of 8.58 Mpc. The quoted uncertainty is based on propagating observational noise rms values through the luminosity calculation. This total CO luminosity includes contributions from NGC 5195. The total molecular mass is  $(9.32 \pm 0.01) \times 10^9 M_\odot$  using the  $\text{H}_2$ -to-CO conversion factor  $\alpha_{\text{CO}} = 4.3 M_\odot / (\text{K km s}^{-1} \text{ pc}^2)$  (Bolatto et al. 2013). The CO luminosity of just NGC 5195 is  $(9.93 \pm 0.01) \times 10^7 \text{ K km s}^{-1} \text{ pc}^2$ , which corresponds to a molecular mass of  $(4.27 \pm 0.04) \times 10^8 M_\odot$ . The CARMA-NRO CO imaging estimated the total mass of NGC 5194 and NGC 5195 to be  $6.0 \times 10^9 M_\odot$  applying the same CO– $\text{H}_2$  conversion factor and distance as used in this study (Koda et al. 2011). Within calibration uncertainties, masking thresholds, and map coverage, our values are also comparable with those of Pety et al. (2013), who derived  $L_{\text{CO}} = 1.8 \times 10^9 \text{ K km s}^{-1} \text{ pc}^2$ , and molecular mass of  $7.9 \times 10^9 M_\odot$  from observations with the IRAM 30 m telescope that covered approximately the same area.

The  $^{12}\text{CO}$ -defined mask is applied to the HCN data from which we produce a velocity-integrated image of HCN emission shown in the right panel of Figure 1. For areas with declinations south of  $47^\circ 07'$  and north of  $47^\circ 15'$ , which include NGC 5195, the HCN noise levels are large due to less data collected near these map edges. These areas are not included in any subsequent analyses presented here. The HCN emission is strong in the central region of M51 but is more patchy and uneven with increasing galactic radius than the CO emission yet still exhibits faint spiral structure in the central  $3' \times 3'$  area. The HCN luminosity over the map area is  $(6.05 \pm 0.08) \times 10^7 \text{ K km s}^{-1} \text{ pc}^2$ . Adopting the conversion factor  $\alpha_{\text{HCN}} = 10 M_\odot / (\text{K km s}^{-1} \text{ pc}^2)$  that assumes self-gravitating dense cores in clouds (Gao & Solomon 2004b), the dense gas mass is  $(6.05 \pm 0.08) \times 10^8 M_\odot$ .

### 3.2. Star Formation Rates

Star formation rates ( $M_\odot/\text{yr}$ ) within M51 are derived from images in the far-ultraviolet (FUV) band measured by GALEX and the MIPS  $24 \mu\text{m}$  band from the Spitzer Space Telescope. In regions of low dust obscuration, massive young stars directly contribute to the observed FUV flux. Newborn stars embedded within regions of moderate to high extinction contribute to the  $24 \mu\text{m}$  flux as their stellar optical and UV radiation heat nearby dust grains that reradiate this energy into the mid- and far-infrared bands. Used together, these bands account for star formation rates from both unobscured and deeply embedded regions of star formation. However, an older stellar population that does not reflect star formation over the last 100 Myr also contributes to the measured luminosities in both the FUV and  $24 \mu\text{m}$  bands. To derive more accurate star formation rates, it is necessary to account for this “cirrus” emission component from the old stellar population in each band.

To evaluate this contribution, we construct three models of the star formation rate. Model 0 is the trivial model, which assumes no contributions to the FUV and  $24 \mu\text{m}$  luminosities from older stars. This model allows a comparison to other studies that also exclude this component (Bigiel et al. 2016; Jiménez-Donaire et al. 2019). The other models consider the distribution of the old stellar component by decomposing the Spitzer image of  $3.6 \mu\text{m}$  surface brightness into galactic structural components using Galfit (Peng et al. 2010). Model 1 follows the example in Peng et al. (2010) for M51 that includes a two-component central bulge and inner and outer spiral arms. We exclude the numerous, bright  $3.6 \mu\text{m}$  emission knots so that each Galfit component more accurately tracks the smooth emission, which limits oversubtractions. Model 2 includes a two-component central bulge and a Sérsic profile that approximates an exponential disk but no spiral-arm structures. In this model, we implicitly assume that the spiral arms are entirely due to young stellar populations, although this



assumption is an oversimplification of current results for spiral structures (Kreckel et al. 2016). In calculating the exponential disk, we exclude pixels located in spiral-arm features (see Figure 3) so as to not bias the fit. For both `Galfit` models, we also simultaneously fit the companion galaxy, M51b, with a two-component central bulge and one spiral-arm component, based on the Peng et al. (2010) models. This avoids biasing the M51a fits in the outer disk and spiral-arm components. The `Galfit` parameters and the 3.6  $\mu\text{m}$  model images for Models 1 and 2 are shown in the Appendix.

The 3.6  $\mu\text{m}$  `Galfit` model intensities are scaled to the FUV and 24  $\mu\text{m}$  bands. The respective scaling factors are determined from the ratio of the median observed FUV and 24  $\mu\text{m}$  intensities to the median model 3.6  $\mu\text{m}$  intensity within several  $5 \times 5$  pixel areas located within interarm regions with no star formation activity. The resultant scaled models are then subtracted from the observed images to remove the old stellar population contributions. For this subtraction, we include only model components where we expect a significant contribution to the FUV and 24  $\mu\text{m}$  intensities from the old stellar populations. For 24  $\mu\text{m}$ , we subtract the normalized bulge and both spiral components for Model 1 and the bulge and disk for Model 2. It is clear from the lack of a significant bulge in the FUV image that the unobscured, central stellar population is old and is contributing little UV flux. So for the FUV, we subtract only the two spiral components for Model 1 and the disk for Model 2. Because Model 2 does not account for spiral-arm features in which older stellar populations are enhanced, its subtraction leads to a positive bias of SFR values. All pixels with negative residuals are set to zero to limit artificial model bias in the SFR maps resulting from the image combination. Using the Aniano et al. (2011) kernels, the corrected 24  $\mu\text{m}$  and FUV images are convolved to the resolution (14  $''$ ) and pixel size (7 $''$ ) of the molecular line data.

For each model, the star formation rate is calculated using the expression by Liu et al. (2011),

$$\text{SFR}(M_{\odot}\text{yr}^{-1}) = 4.6 \times 10^{-44} [L(\text{FUV}) + 6.0L(24\mu\text{m})], \quad (2)$$

where the luminosities are in  $\text{erg s}^{-1}$ . This calibration assumes a Kroupa (2001) stellar IMF to account for newly formed low-mass stars that do not significantly contribute to the FUV and 24  $\mu\text{m}$  emission. The uncertainty of SFR is  $1.33 \times 10^{-5} M_{\odot} \text{yr}^{-1}$ , which is derived from the standard deviation of the background areas in both the FUV and 24  $\mu\text{m}$  images and propagated through Equation (2).

We acknowledge that our method to quantify the old stellar population contributions to the star formation tracers is complicated and depends on the accuracy of the decomposition of the 3.6  $\mu\text{m}$  image by `Galfit` as well as the scaling of the model 3.6  $\mu\text{m}$  surface brightness values to the FUV and 24  $\mu\text{m}$  bands. Alternatives to account for the cirrus emission include unsharp masking to identify a diffuse component produced by radiation from the old stellar population (Rahman et al. 2011) and direct modeling of the cirrus emission from radiation fields and dust emissivities (Leroy et al. 2012). Our method offers a more physically based alternative to unsharp masking as `Galfit` identifies galactic components that are expected to be populated by older stars.

### 3.3. Stellar-mass Surface Density

The mass of the stellar component is derived using the method described by Zibetti et al. (2009). In brief,  $g$ -,  $i$ -, and  $H$ -band images are resampled to the 3.6  $\mu\text{m}$  image pixel size and coverage. Background and foreground objects identified in the 3.6  $\mu\text{m}$  image are removed in the  $g$ ,  $i$ , and  $H$  images by interpolation. The  $g$  and  $i$  images are convolved to the 2 $''$  resolution of the  $H$ -band data, and all images are converted to Jy/pixel surface brightness units. Each image is adaptively smoothed to achieve signal-to-noise ratios greater than 20 using the code of Zibetti (2009). For a given pixel, the largest smoothing element is selected and applied to the remaining images in order to match the spatial resolution. In all cases across the disk of M51, the  $H$ -band data required the largest smoothing kernel. The  $g-i$  and  $i-H$  colors are derived for each pixel and are corrected for galactic foreground extinction assuming  $A_v=0.096$  (Schlafly & Finkbeiner 2011). From the colors, the median mass-to-light ratio at the  $H$  band,  $\Psi_H$ , is determined based on the look-up tables of Zibetti et al. (2009) that are based on the Bruzual & Charlot (2003) stellar population synthesis models. For pixels with colors outside the look-up table limits, values for  $\Psi_H$  are interpolated from valid, neighboring pixel values.  $H$ -band luminosities,  $L_H$ , are calculated from the adaptively smoothed  $H$ -band image using a distance of 8.58 Mpc. We convert these luminosities to “in-band” solar units using  $L_{\odot,H} = 1.08 \times 10^{33} \text{ erg s}^{-1}$ , derived from the absolute Vega magnitude of the Sun in the 2MASS  $H$  band and the flux zero-point listed in Willmer (2018). The stellar-mass image is  $L_H\Psi_H$ . The resultant stellar-mass image is then smoothed and resampled to the pixel size and resolution of the molecular line data.

The primary advantage of using the  $H$  band to derive stellar masses is that the method does not require a subtraction of an extended, warm-dust component that is heated by star formation activity as is the case at 3.6 $\mu\text{m}$  (Meidt et al. 2012; Querejeta et al. 2015), which can introduce additional uncertainties in the final result. However, owing to the low signal-to-noise ratio of the 2MASS  $H$ -band data in the outer regions of the disk, this band is not as useful as the highly sensitive 3.6  $\mu\text{m}$  image for decomposing the galaxy into structural components using `Galfit` as described in Section 3.2.

## 4. Dense Gas Mass Fraction in the Molecular Cloud Population of M51

The distribution of high-density ( $>10^4 \text{ cm}^{-3}$ ) regions within molecular clouds provides a roadmap for both ongoing star formation and star formation activity to occur within several freefall times of the dense gas. Integrated over the projected area of a cloud or an ensemble of clouds, the dense gas mass fraction can offer a measure of future star formation efficiency assuming other conditions are satisfied such as self-gravitating clumps and cores and a fixed fraction of dense gas redistributed into stars. We define the dense gas fraction as the ratio of cloud mass residing in gas configurations with number densities greater than  $n'$  to the total cloud mass,

$$f_{\text{DG}}(n>n') = M(n>n')/M_{\text{TOT}}, \quad (3)$$

where  $n'$  is a threshold volume density appropriate for the dense gas tracer. For a single, spectral line high-density gas

tracer such as the HCN  $J = 1 - 0$  line used in this study, this expression assumes a small contribution to the dense gas mass from regions with densities much larger than the critical density required to collisionally excite the molecules into the upper energy level of the transition. The measured  $f_{\text{DG}}$  value represents a luminosity-weighted average of the dense gas mass fraction for the set of molecular clouds within the telescope beam or over the area subtended by the stacking condition (see Section 4.1).

The HCN-to-CO intensity ratio has been widely applied as a measure of the dense gas fraction in Galactic molecular clouds (Jackson et al. 1996; Helfer & Blitz 1997; Paglione et al. 1998; Evans et al. 2020). The CO luminosity provides an estimate of the bulk mass of molecular clouds while the HCN  $J = 1 - 0$  line (or higher rotational transitions) tracks the mass of the higher-volume-density component within a cloud. Specifically,

$$f_{\text{DG}}(n > n') = \frac{M_{\text{dense}}}{M_{\text{mol}}} = \frac{\alpha_{\text{HCN}} L_{\text{HCN}}}{\alpha_{\text{CO}} L_{\text{CO}}} = (2.3 \pm 1.3)R, \quad (4)$$

where  $R$  is the observed HCN-to-CO ratio of luminosities and the  $\text{H}_2$  component with low CO abundances in diffuse gas is not included. The coefficient and uncertainty terms in Equation (4) assume  $\alpha_{\text{CO}} = 4.3 M_{\odot}/(\text{K km s}^{-1} \text{pc}^2)$ ,  $\alpha_{\text{HCN}} = 10 M_{\odot}/(\text{K km s}^{-1} \text{pc}^2)$ , and fractional uncertainties of 0.3 (Bolatto et al. 2013) and 0.5, respectively. This optimistic conversion error still exceeds any measurement errors to derive  $R$  and so the fractional uncertainties of  $f_{\text{DG}}$  are greater than  $>75\%$ . We apply this factor for all conversions of  $R$  to  $f_{\text{DG}}$  in Sections 4.1.1, 4.1.2, 5.3, and 6.

The appropriate volume density threshold,  $n'$ , for the HCN  $J = 1 - 0$  line depends on several factors. The critical density,  $n_c$ , of an emission line is the density at which the rate of collisional excitations equals the spontaneous decay rate. For the HCN  $J = 1 - 0$  line,  $n_c = 5 \times 10^5 \text{ cm}^{-3}$  in the limit of optically thin emission and collisions with  $\text{H}_2$  molecules and temperature of 10–20 K (Shirley 2015). This density is comparable to the mean density of prestellar and protostellar cores, which makes this line so attractive as a dense gas tracer. However, observations of the HCN  $J = 1 - 0$  line in the Milky Way demonstrate that the line is often optically thick so one must account for radiative trapping and its impact on line excitation to derive an effective critical density. For the HCN line, this effective critical density is  $\sim(3-10) \times 10^3 \text{ cm}^{-3}$  for kinetic temperatures less than 20 K, varying column densities and HCN abundances, and collisions with  $\text{H}_2$  molecules (Helfer & Blitz 1997; Paglione et al. 1998; Shirley 2015). These densities are more similar to the dense clumps and filaments within molecular clouds rather than to the prestellar or protostellar cores. In addition, Goldsmith & Kauffmann (2017) demonstrate that in low-density environments with high ionization fractions, such as envelopes of molecular clouds or in the central regions of galaxies, electron collisions can also impact the HCN excitation, which can further decrease the effective critical density of the HCN  $J = 1 - 0$  line. Goicoechea et al. (2022) find similar results when electron collisions dominate the excitation of the HCN molecules. For this study, we adopt the value of  $n' = 10^4 \text{ cm}^{-3}$  for the HCN  $J = 1 - 0$  transition that assumes a mixture of optically thin and thick emission and no electron excitation. For the optically thick CO emission, radiative trapping maintains sufficient excitation such that the effective critical density is  $\sim 100 \text{ cm}^{-3}$ .

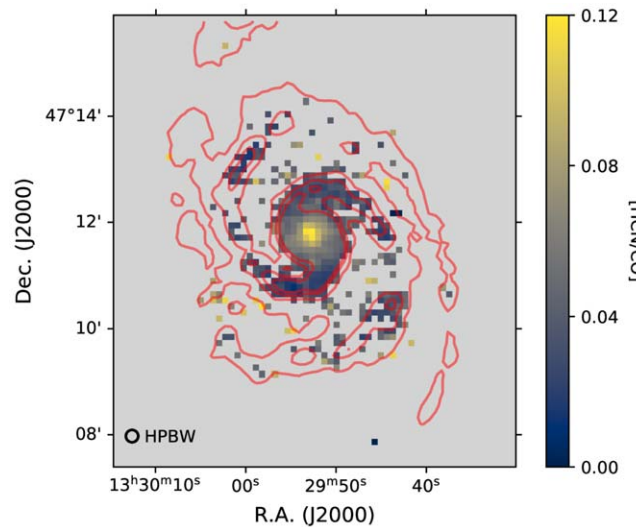


**Figure 2.** Image of the HCN/CO ratio at  $14''$  angular resolution. Only pixels with HCN-to-CO ratios greater than  $3\sigma$  are shown. Red contours show the  $^{12}\text{CO } J = 1 - 0$  integrated intensities to delineate spiral-arm features. The contour levels are 5, 15, 25, and  $35 \text{ K km s}^{-1}$ .

To examine the dense gas fraction in M51, we calculate  $R$  for each  $7''$  pixel in the matched HCN and CO images of integrated intensity and propagate intensity uncertainties to derive  $\sigma(R)$ . The sensitivity of  $R$  is limited by the much weaker HCN emission. The image of  $R$  is shown in Figure 2, where we have clipped pixels with  $R/\sigma(R)$  less than 3. The red contours show the distribution of  $W(^{12}\text{CO})$  that traces the spiral structure. The highest ratios ( $R > 0.08$ ) are found in the central bulge area of M51. Beyond the extent of the bulge, spatially coherent features of  $R$  follow the inner spiral arms. There are marginal detections of  $R$  in a few locations between the spiral arms.

#### 4.1. Spectral Stacking

The HCN-to-CO ratio can be probed to fainter levels of the HCN emission than the  $3\sigma$  limits of  $R$  shown in Figure 2 by stacking the HCN and  $^{12}\text{CO}$  spectra selected by a common physical attribute or spatial grouping. The stacked spectra represent the average of the ensemble that satisfy the selection criteria. This spectral stacking method has been applied to HCN data by Bigiel et al. (2016) and Jiménez-Donaire et al. (2019), where HCN spectra are stacked in bins of galactic radius or stellar surface density.

##### 4.1.1. Bulge and Spiral-arm Regions of Interest

The deep gravitational potential of spiral arms provides an environment that could impact the dense gas fractions of the molecular cloud population. To explore this role, we define regions of interest (ROI) in the  $3.6 \mu\text{m}$  image as polygons that circumscribe segments along both spiral arms and interarm regions. We also define the M51 bulge as a distinct ROI that includes the area within a circular radius of  $35''$ . Finally, all CO and HCN spectra within the CO-defined mask (5997 pixels) are stacked to produce globally averaged spectra (ROI 14). The top-left panel of Figure 3 shows the labels for all the ROIs, which are also grouped into separate arms and interarms distinguished by color.

For each ROI, we identify the set of pixels that fall within the subtended area. In the case where the distance between the

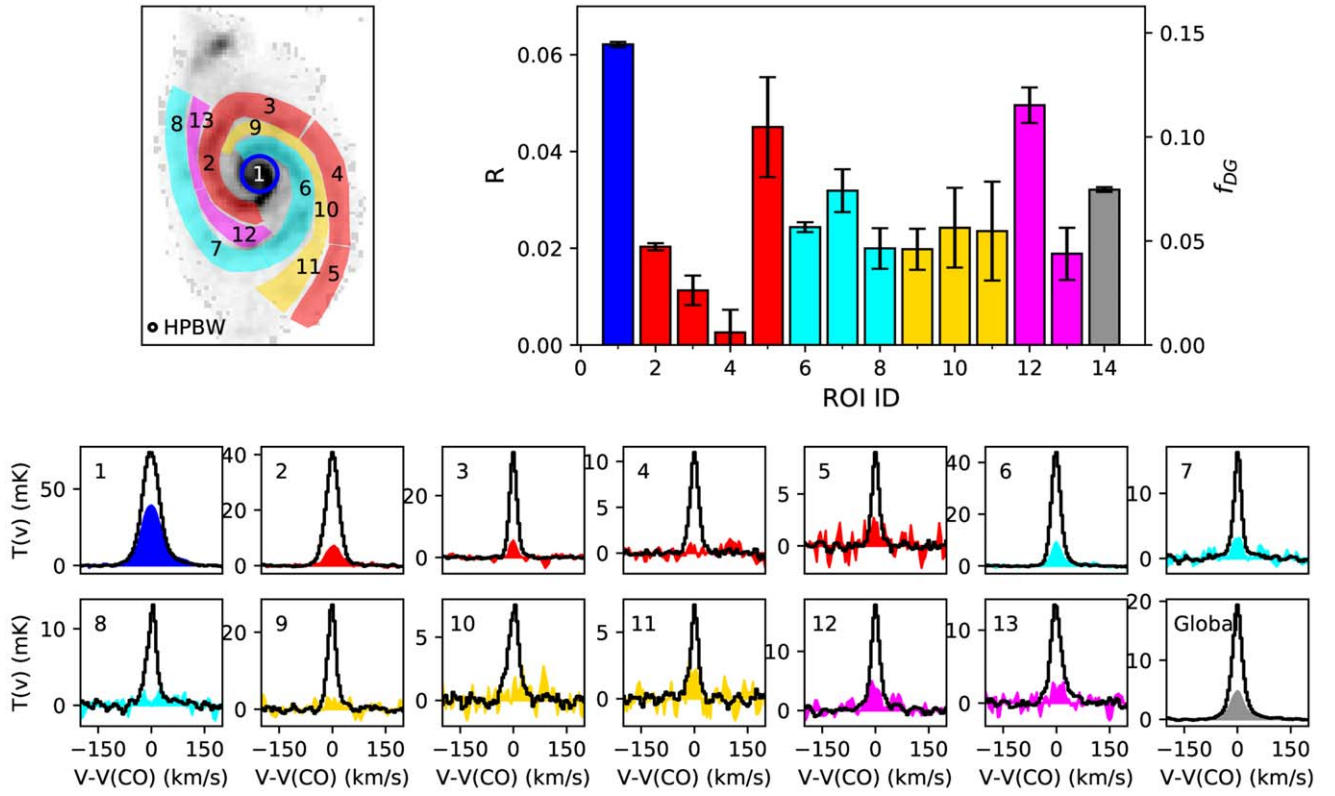


**Figure 3.** (Top left) Image of the  $^{12}\text{CO } J=1-0$  integrated intensity and ROIs corresponding to the central bulge (blue circle), spiral-arm segments (red and cyan shading), and interarm segments (yellow and magenta shading). (Bottom) Stacked  $^{12}\text{CO}$  (black and divided by 10) and HCN spectra (colored according to group) for each ROI. The global CO and HCN spectra correspond to the stacked CO and HCN spectra (gray) for all pixels with detected  $^{12}\text{CO}$  emission. (Top right) Ratio of HCN to CO luminosities (left axis) and  $f_{\text{DG}}$  (right axis) derived from stacking CO and HCN emission in each ROI. Error bars refer to uncertainties in  $R$  values. The gray bar (ROI 14) is the global HCN/CO value.

**Table 1**  
ROI Stacked Spectra Properties

ROI	Npix	(v1,v2) (km s $^{-1}$ )	W(HCN) (K km s $^{-1}$ )	$\sigma$ (W(HCN)) (K km s $^{-1}$ )	W(CO) (K km s $^{-1}$ )	$\sigma$ (W(CO)) (K km s $^{-1}$ )	$R$	$\sigma$ ( $R$ )	$f_{\text{DG}}$	$\sigma$ ( $f_{\text{DG}}$ )
1	69	[-125, 125]	2.982	0.025	48.014	0.102	0.062	0.001	0.144	0.084
2	188	[-90, 90]	0.376	0.014	18.500	0.070	0.020	0.001	0.047	0.028
3	158	[-75, 75]	0.100	0.027	8.803	0.074	0.011	0.003	0.026	0.015
4	199	[-50, 50]	0.009	0.016	3.357	0.056	0.003	0.005	0.006	0.004
5	144	[-50, 50]	0.104	0.024	2.306	0.062	0.045	0.010	0.105	0.061
6	262	[-75, 75]	0.366	0.015	15.018	0.064	0.024	0.001	0.057	0.033
7	215	[-70, 70]	0.155	0.021	4.847	0.083	0.032	0.004	0.074	0.043
8	105	[-70, 70]	0.094	0.020	4.704	0.110	0.020	0.004	0.046	0.027
9	61	[-60, 60]	0.160	0.034	8.083	0.128	0.020	0.004	0.046	0.027
10	67	[-65, 65]	0.068	0.023	2.796	0.087	0.024	0.008	0.056	0.033
11	139	[-60, 60]	0.045	0.019	1.897	0.077	0.024	0.010	0.055	0.032
12	96	[-75, 75]	0.293	0.021	5.911	0.118	0.050	0.004	0.115	0.067
13	69	[-80, 80]	0.102	0.029	5.420	0.104	0.019	0.005	0.044	0.026
14	5997	[-125, 125]	0.049	0.001	1.522	0.007	0.032	0.000	0.075	0.044

pixel position and the nearest ROI boundary is less than  $7''$ , corresponding to half of the HPBW, we do not correct for the signal gathered by the telescope beam that extends beyond the ROI boundary. To stack the data, the velocity axis for each selected spectrum in the ROI is shifted to be centered at  $0 \text{ km s}^{-1}$  by subtracting the velocity centroid of the CO spectrum at the same position. This relative spectrum is sampled between  $-200$  and  $+200 \text{ km s}^{-1}$  with a  $5 \text{ km s}^{-1}$  spectral resolution and coadded to the stacked spectrum with a  $1/\sigma^2$  weighting. The bottom subplot in Figure 3 shows the stacked  $^{12}\text{CO}$  and HCN

spectra. The HCN spectra are colored according to the ROI groupings.

The resultant stacked  $^{12}\text{CO}$  and HCN spectra are integrated over velocities where CO is detected in the stacked spectrum. The rms values of the stacked spectra are derived from the standard deviation of intensities outside of these velocity intervals. The HCN-to-CO ratio is calculated from the ratio of HCN-to-CO integrated intensities. Table 1 summarizes the selected velocity intervals, measured intensities, ratios, and uncertainties for each ROI.



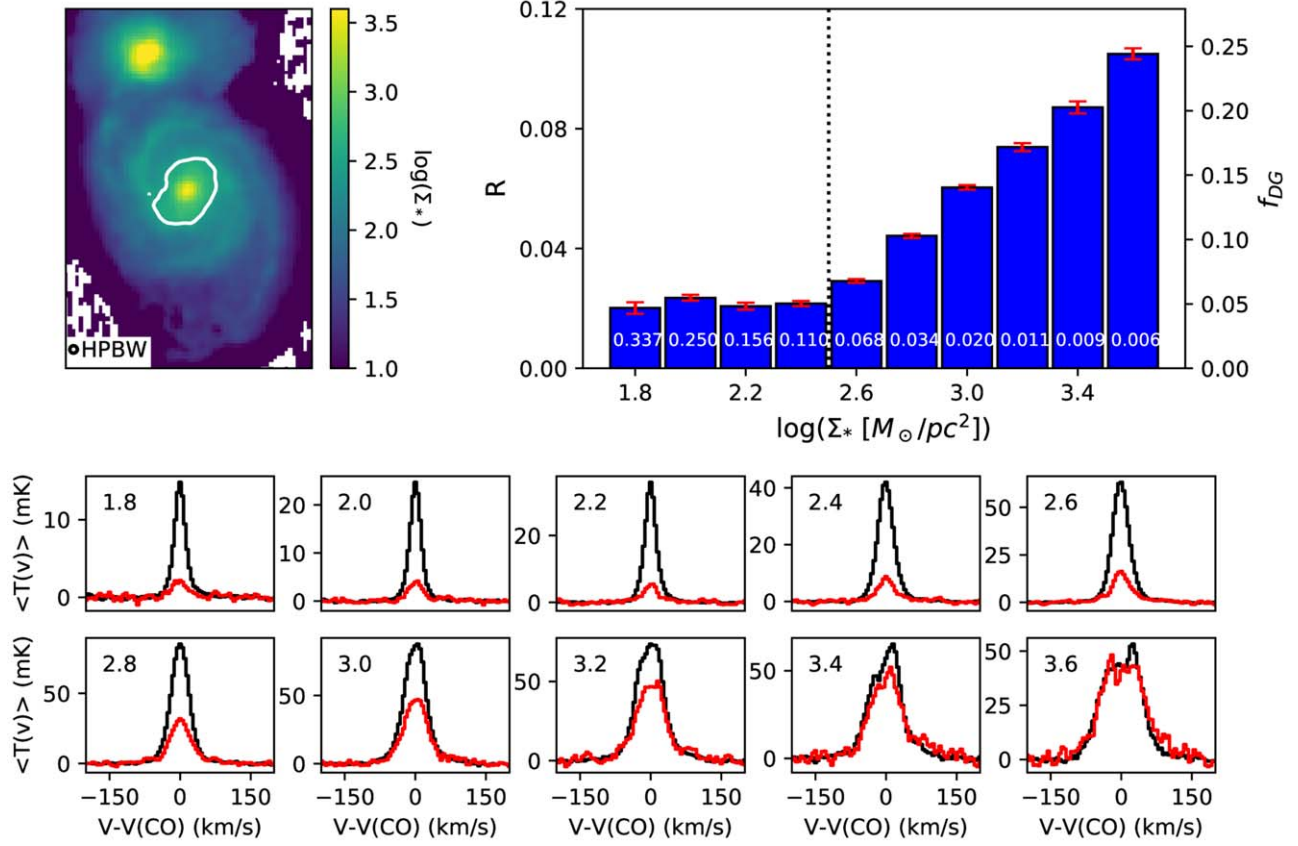


**Figure 4.** (Top left) Image of the stellar-mass surface density derived from the 2MASS  $H$ -band image and a varying mass-to-light ratio based on  $g - i$  and  $i - H$  colors (Zibetti et al. 2009). The white contour denotes  $\log(\Sigma_*) = 2.5$ . (Top right) HCN-to-CO luminosity ratio (left axis) and the dense gas fraction,  $f_{DG}$  (right axis) in each bin of stellar-mass surface density. Values in each bin reflect the fractional area covered. The vertical dotted line marks the transition at  $\log(\Sigma_*)$  to higher  $f_{DG}$  values with increasing stellar mass in the central bulge. (Bottom) Stacked  $^{12}\text{CO}$  (black and divided by 10) and HCN spectra (red) for each stellar-mass bin. The number in each box is  $\log(\Sigma_*)$  for that bin.

$^{12}\text{CO}$  emission is readily detected in all ROIs that span most of the bulge and disk areas of M51—including all of the interarm regions. The ubiquity of CO in the stacked spectra is expected given that all of the ROI areas fall within the CO-defined mask described in Section 3.1. From extinction features within high-resolution, optical images obtained with the Hubble Space Telescope (HST) and  $8\ \mu\text{m}$  emission features from Spitzer, the interarm regions of M51 contain narrow spiral spurs of material that stretch between adjacent spiral-arm segments. These molecular features are not resolved by the  $^{12}\text{CO}$  data presented in this study but are evident in the Plateau de Bure Interferometer Arcsecond Whirlpool Survey (PAWS)  $^{12}\text{CO}$  image of M51 (Schinnerer et al. 2013). Such spiral spurs emerge from the gas subjected to increased velocity shear in the interarm regions (Kim & Ostriker 2002). In M51, molecular clouds residing within these spurs are not destroyed by the high-velocity shear of the interarm regions but maintain sufficient column densities for self-shielding to remain in the molecular gas phase throughout their transit through the interarm region to the next spiral arm (Koda et al. 2009). HCN emission is detected with signal to noise greater than 3 within most ROIs. It is not detected at this level in ROIs 4, 10, and 11.

The top-right subplot of Figure 3 displays the  $R$  values (left axis) and  $f_{DG}$  values (right axis). The error bars correspond to uncertainties in  $R$ . The large values of  $R$  and  $f_{DG}$  in the M51 bulge have been previously established in earlier studies (Bigiel et al. 2016; Gallagher et al. 2018; Jiménez-Donaire et al. 2019;

Querejeta et al. 2019). Within the uncertainties, there is little variation of  $f_{DG}$  between spiral arms and interarms. The dense gas fraction averaged over all spiral-arm and interarm segments are 0.051 and 0.063, respectively. The comparable values of  $f_{DG}$  are unexpected given the deeper gravitational potential that defines the spiral arms. We discuss this limited range in  $f_{DG}$  values in more detail in Section 6.2.

#### 4.1.2. Stellar-mass Surface Density

The scale height of the molecular ISM in galaxies is small in comparison to the distribution of stars and atomic gas. Consequently, molecular clouds are subject to the effective pressure generated by the weight of the stellar, gas, and dark matter components residing above and below the disk midplane. Such pressure facilitates the transition of warm, neutral, atomic gas into the cold, neutral, atomic gas phase, which is often a precursor to the formation of molecular clouds (Elmegreen 1993). Can such pressure also impact the development of high-density gas within molecular clouds?

Previous studies of HCN and CO in nearby galaxies have already demonstrated a relationship between  $f_{DG}$  and the mass surface density of stars as well as the full pressure component,  $P \propto \Sigma_{\text{gas}} \Sigma_*$  (Gallagher et al. 2018; Jiménez-Donaire et al. 2019). Here, we examine the relationship of the dense gas fraction with stellar-mass surface density using spectral stacking. Figure 4 shows the stacked HCN and CO spectra for each  $\log(\Sigma_*)$  bin. Table 2 summarizes the integrated

**Table 2**  
Stellar-mass Surface Density Stacked Spectra Properties

$\log(\frac{\Sigma_*}{M_\odot \text{pc}^{-2}})$	Npix	(v1,v2) (km s <sup>-1</sup> )	W(HCN) (K km s <sup>-1</sup> )	$\sigma$ (W(HCN)) (K km s <sup>-1</sup> )	W(CO) (K km s <sup>-1</sup> )	$\sigma$ (W(CO)) (K km s <sup>-1</sup> )	$R$	$\sigma(R)$	$f_{\text{DG}}$	$\sigma(f_{\text{DG}})$
1.8	891	[-80,80]	0.096	0.009	4.794	0.051	0.020	0.002	0.047	0.027
2.0	661	[-80,80]	0.184	0.008	7.805	0.050	0.024	0.001	0.055	0.032
2.2	413	[-80,80]	0.244	0.014	11.742	0.046	0.021	0.001	0.048	0.028
2.4	290	[-80,80]	0.398	0.016	18.408	0.068	0.022	0.001	0.050	0.029
2.6	179	[-90,90]	0.860	0.019	29.466	0.087	0.029	0.001	0.068	0.040
2.8	91	[-100,100]	1.890	0.029	42.737	0.158	0.044	0.001	0.103	0.060
3.0	52	[-105,105]	3.249	0.039	53.789	0.216	0.060	0.001	0.140	0.082
3.2	28	[-140,140]	4.091	0.074	55.390	0.212	0.074	0.001	0.172	0.100
3.4	23	[-140,140]	4.427	0.096	50.800	0.397	0.087	0.002	0.203	0.118
3.6	16	[-150,150]	5.380	0.091	51.246	0.285	0.105	0.002	0.244	0.142

intensities and ratios derived from the stacked spectra. Within the disk, where  $\log(\Sigma_*) < 2.5$ , which contains 85% of the area over all bins,  $f_{\text{DG}}$  is  $\sim 0.05$  with little variation over the  $\log(\Sigma_*)$  range of 1.8 to 2.4. For  $\log(\Sigma_*) > 2.5$ , corresponding to much of the stellar bulge component, the dense gas mass fraction rapidly rises. Evaluating the dense gas fraction within 1 kpc wide bins of radius shows a similar constant value of  $\sim 0.05$  for radii between 2 and 8 kpc and a steep rise to 0.18 in the central 2 kpc. Both Bigiel et al. (2016) and Jiménez-Donaire et al. (2019) find similar profiles of  $f_{\text{DG}}$  with galactic radius.

## 5. Star Formation Scaling Relationships

The Kennicutt–Schmidt (KS) scaling relationship connects the star formation rate with the amount of neutral gas mass (atomic, molecular, or both) (Schmidt 1959; Kennicutt 1989, 1998). It has been applied to disk-averaged values of  $\Sigma_{\text{SFR}}$  and  $\Sigma_{\text{gas}}$  for a large set of galaxies (Kennicutt 1989; de los Reyes & Kennicutt 2019) and resolved measures of  $\Sigma_{\text{SFR}}$  and  $\Sigma_{\text{gas}}$  values within a galaxy (Kennicutt et al. 2007; Bigiel et al. 2008; Leroy et al. 2008). The KS relationship is expressed as a power law,  $\Sigma_{\text{SFR}} = A(\Sigma_{\text{gas}})^N$ , whose parameters,  $A$  and  $N$ , and the measured scatter provide important constraints to the evolution of the ISM and pathways to star formation within the varying gas environments of galaxies (Kennicutt & Evans 2012).

### 5.1. $\Sigma_{\text{SFR}}$ and $\Sigma_{\text{mol}}$

M51 has been a primary target of studies exploring the resolved KS relationship between  $\Sigma_{\text{SFR}}$  and  $\Sigma_{\text{mol}}$  with varying results (Kennicutt et al. 2007; Bigiel et al. 2008; Liu et al. 2011; Chen et al. 2015; Bigiel et al. 2016; Leroy et al. 2017). These differences arise in part due to angular resolutions and whether the analysis accounts for contributions from an older ( $> 100$  Myr) stellar population to the star formation tracer (Liu et al. 2011). In the top row of Figure 5, we show the KS relationship between  $\Sigma_{\text{SFR}}$  and  $\Sigma_{\text{mol}} = \alpha_{\text{CO}} \int dvT(\text{CO}) M_\odot \text{pc}^{-2}$  derived for the three SFR models presented in Section 3.2. Data with  $\log(\Sigma_{\text{SFR}})$  less than  $-9.5$  are excluded as the conversion to the star formation rate for these faint FUV and 24  $\mu\text{m}$  luminosities is less reliable (Leroy et al. 2012). We fit for the parameters  $A$  and  $N$  in the expression,  $\log(\Sigma_{\text{SFR}}) = A + N \log(\Sigma_{\text{mol}})$  using bisector least squares in the Python module `bces` (Nemmen et al. 2012) that is based on Akritas & Bershady (1996). We also calculate the posterior probability distribution for the set of regression parameters (denoted  $A_B$ ,  $N_B$ ) using the `emcee` package (Foreman-Mackey et al. 2013).

Table 3 lists the best-fit values for  $A$  and  $N$ , uncertainties, and scatter derived from the bisector fit and the  $\pm 2\sigma$  range from the posterior distributions of  $A_B$  and  $N_B$ . The bisector fits show the same trend identified by Liu et al. (2011) in which the power-law index is near unity for SFR not corrected for contributions from the older stellar population as in Model 0. For corrected SFR values (Model 1 and Model 2), the index steepens to 1.2. The Bayes’ regression shows values of the slope posterior distributions to be linear or marginally sublinear for all three SFR models. Shetty et al. (2013) applied hierarchical Bayesian regression on surface densities of star formation rates and molecular gas for a set of galaxies, including M51, for which they found a strongly sublinear slope of 0.72 with a  $\pm 2\sigma$  range [0.62, 0.83] over a narrower range of  $\Sigma_{\text{mol}}$  and fewer points than the data used in this study.

### 5.2. $\Sigma_{\text{SFR}}$ and $\Sigma_{\text{dense}}$

The variation of the SFR with the dense gas mass is also an important relation as it probes the localized volumes of gas more spatially connected to star formation over the ensemble of clouds within the resolution element of the observations. The increased angular resolution of the LMT relative to other single-dish telescopes provides sensitivity to the range of HCN luminosities  $5 \times 10^4$ – $10^6$  K km s<sup>-1</sup> pc<sup>2</sup>, which is not well populated from previous studies. The LMT data complement the recent Northern Extended Millimeter Array (NOEMA) measurements that are also sensitive to this HCN luminosity range (Querejeta et al. 2019).

The bottom row of Figure 5 shows the relationship between  $\Sigma_{\text{SFR}}$  and  $\Sigma_{\text{dense}} = \alpha_{\text{HCN}} \int dvT(\text{HCN}) M_\odot \text{pc}^{-2}$  for each SFR model in the form of a two-dimensional histogram. Only points with  $\Sigma_{\text{SFR}}$  greater than  $-9.5$  are considered. We apply both bisector and Bayes’ regression to the expression  $\log(\Sigma_*) = A + N \log(\Sigma_{\text{dense}})$  and summarize the results in Table 3. Sublinear relationships are derived for SFR Models 1 and 2 with slopes  $\sim 0.65$  (bisector) and a  $2\sigma$  posterior distributions range between 0.50 and 0.68 from the Bayes’ regression.

### 5.3. Star Formation Efficiency and $\Sigma_*$

One of the key results to emerge from the EMPIRE survey is the anticorrelation of the star formation efficiency of dense gas,  $\text{SFE}_{\text{dense}} = \Sigma_{\text{SFR}}/\Sigma_{\text{dense}}$ , with the local environment properties: stellar-mass surface density, molecular gas surface density, molecular gas fraction, and the midplane pressure (Gallagher et al. 2018; Jiménez-Donaire et al. 2019). From three NOEMA fields of M51 with a high angular resolution,

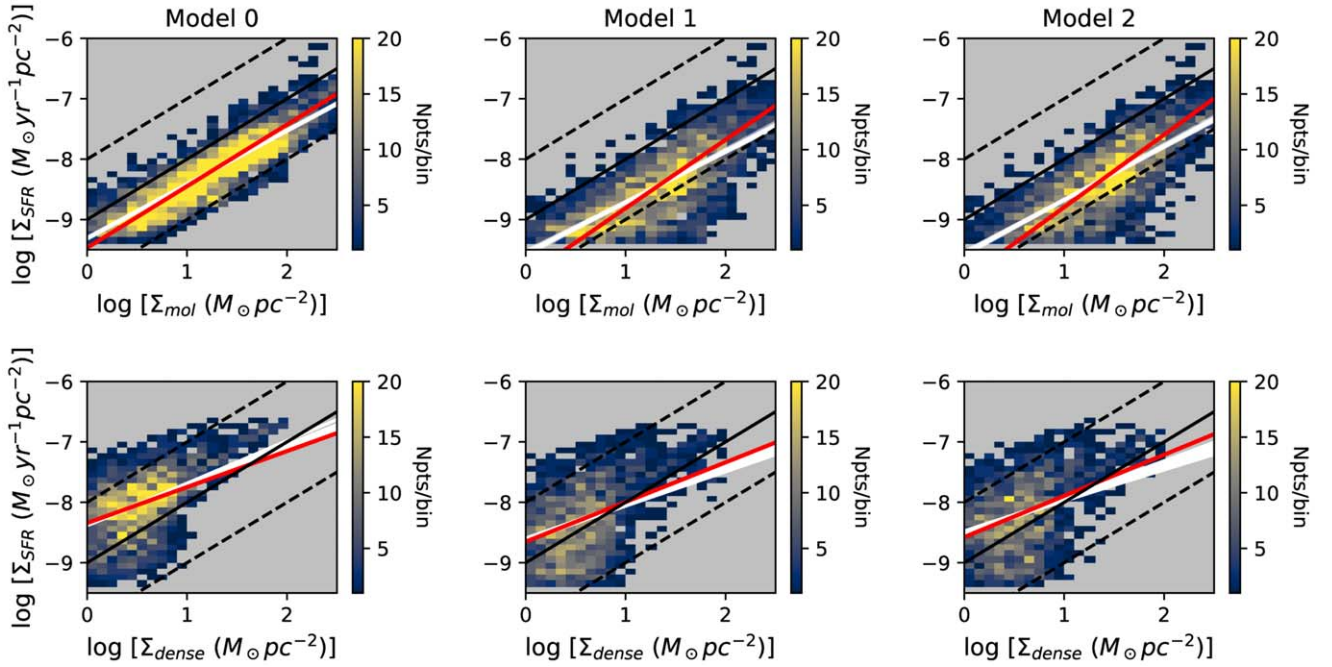


**Figure 5.** (Top row) Variation of  $\Sigma_{\text{SFR}}$  with  $\Sigma_{\text{mol}}$  for star formation rates calculated for (left) Model 0, (middle) Model 1 and (right) Model 2. Images are two-dimensional histograms of  $\log(\Sigma_{\text{SFR}})$  and  $\log(\Sigma_{\text{mol}})$ . Solid red lines show the fit to all individual data points using the bisector least-squares method. The white solid lines show the model derived from 32 random draws of the slope and y-intercept posterior distributions. The black lines show the molecular gas depletion times from top to bottom of  $10^8$ ,  $10^9$ , and  $10^{10}$  yr. (Bottom row) Two-dimensional histogram showing the variation of  $\Sigma_{\text{SFR}}$  with  $\Sigma_{\text{dense}}$  for each SFR model. The red line represents the bisector fit to the data, and the white lines show the Bayes' regression results from 32 random draws of the posterior distributions.

**Table 3**  
Model Parameters  $\log(\Sigma_{\text{SFR}}) = A + N \log(\Sigma_X)$

SFR Model	X	A	N	$\sigma$	$A_B (\pm 2\sigma)$	$N_B (\pm 2\sigma)$
0	mol	-9.48 (0.01)	1.03 (0.01)	0.28	[-9.34, -9.30]	[0.88, 0.91]
1	mol	-10.00 (0.02)	1.16 (0.01)	0.46	[-9.66, -9.58]	[0.84, 0.89]
2	mol	-10.06 (0.02)	1.23 (0.01)	0.46	[-9.69, -9.60]	[0.90, 0.96]
0	dense	-8.34 (0.01)	0.60 (0.01)	0.47	[-8.39, -8.34]	[0.61, 0.68]
1	dense	-8.65 (0.01)	0.66 (0.01)	0.54	[-8.65, -8.58]	[0.54, 0.63]
2	dense	-8.58 (0.01)	0.68 (0.01)	0.56	[-8.54, -8.47]	[0.50, 0.60]

Querejeta et al. (2019) also identify an anticorrelation but with a large scatter of points for a given  $\Sigma_*$ . The authors connect this trend to the Central Molecular Zone (CMZ) of the Milky Way, where there is a large reservoir of dense gas and a large dense gas fraction (Jackson et al. 1996; Jones et al. 2012) but a suppressed star formation rate relative to the disk (Longmore et al. 2013; Kruijssen et al. 2014; Barnes et al. 2017; Lu et al. 2019).

To examine this dependence in our data, we apply spectral stacking within logarithmic bins of  $\Sigma_*$  as in Figure 4 to evaluate  $\Sigma_{\text{SFR}}$ ,  $\Sigma_{\text{dense}}$ , and  $\Sigma_{\text{mol}}$ . For a given  $\log(\Sigma_*)$  bin, the star formation efficiencies are

$$\text{SFE}_{\text{dense}}(\text{Myr}^{-1}) = 10^6 \frac{\Sigma_{\text{SFR}}(M_{\odot} \text{pc}^{-2} \text{yr}^{-1})}{\alpha_{\text{HCN}} \int dv \langle T(\text{HCN}) \rangle} \quad (5)$$

and

$$\text{SFE}_{\text{mol}}(\text{Myr}^{-1}) = 10^6 \frac{\Sigma_{\text{SFR}}(M_{\odot} \text{pc}^{-2} \text{yr}^{-1})}{\alpha_{\text{CO}} \int dv \langle T(\text{CO}) \rangle}, \quad (6)$$

where  $\Sigma_{\text{SFR}} = \sum_{k=1}^{N_b} \text{SFR}_k / \sum_{k=1}^{N_b} A_k$ ,  $A_k$  is the area per pixel in  $\text{pc}^2$ ,  $N_b$  is the number of pixels within the  $\log(\Sigma_*)$  bin, and  $\langle T(\text{HCN}) \rangle$  and  $\langle T(\text{CO}) \rangle$  are the stacked HCN and CO spectra, respectively.

Figure 6 shows the variation of the dense gas (red points) and molecular (blue points) star formation efficiencies with  $\log(\Sigma_*)$  and the  $R$  calculated within each  $\log(\Sigma_*)$  bin for the 3 SFR models. As found for many galaxies in the EMPIRE sample including M51, there is an overall decreasing relationship of  $\text{SFE}_{\text{dense}}$  with increasing  $\Sigma_*$  and  $R$ . However, these profiles are not well described by a power law but, rather, exhibit a broad inflection point over the  $\log(\Sigma_*)$  range 2.5–3.0. A similar inflection point is seen in the data presented by Gallagher et al. (2018) for M51. This inflection point is coincident with the stellar-mass surface density at which  $f_{\text{DG}}$  increases (see Figure 4).  $\text{SFE}_{\text{mol}}$  shows a mostly flat (Model 0) or slight decreasing (Models 1 and 2) profile with increasing  $\Sigma_*$  and  $f_{\text{DG}}$  that is consistent with a linear or slightly sublinear relationship between  $\Sigma_{\text{SFR}}$  and  $\Sigma_{\text{mol}}$ .

## 6. Discussion

### 6.1. Comparison to the Milky Way

It is useful to compare these results on M51 with similar measures of  $f_{\text{DG}}$  in the Milky Way where the improved spatial resolution enables one to pinpoint the areas within a cloud responsible for the HCN emission. Jackson et al. (1996) and



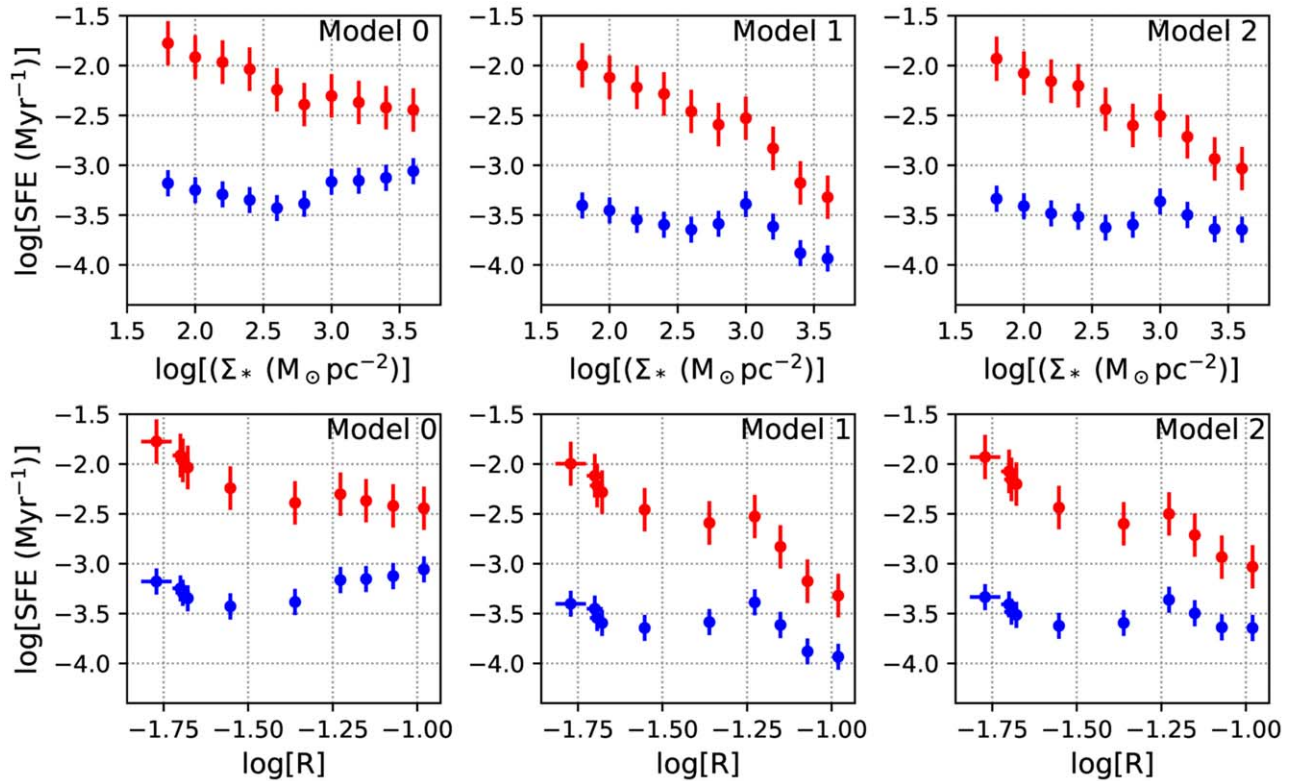


**Figure 6.** (Top row) Variation of star formation efficiencies for dense (red) and molecular (blue) gas within bins of stellar-mass surface density for each SFR model described in Section 3.2. (Bottom row) Star formation efficiency of dense and molecular gas with the ratio of HCN-to-CO luminosities derived in bins of stellar-mass surface density. Error bars mostly reflect the assumed uncertainties in  $\alpha_{\text{CO}}$  and  $\alpha_{\text{HCN}}$ .

Jones et al. (2012) imaged the HCN and CO  $J = 1 - 0$  emission from the CMZ of the Galaxy. The well-known radio features, Sgr A and Sgr B, are bright in HCN emission but there is extended HCN emission throughout the CMZ that is distributed over a large velocity interval of  $\pm 200 \text{ km s}^{-1}$ . Averaged over the 500 pc aperture, comparable to the spatial resolution in this study, Jackson et al. (1996) derive an HCN-to-CO ratio of 0.06 corresponding to  $f_{\text{DG}} = 0.14$ . Integrating over the entire CMZ, Jones et al. (2012) measure a higher value of  $R = 0.095$ , which scales to  $f_{\text{DG}} = 0.22$ . Figure 2 shows  $\text{HCN}/\text{CO} = 0.12$ ,  $f_{\text{DG}} = 0.28$  in the nucleus of M51, and  $\text{HCN}/\text{CO} > 0.056$  ( $f_{\text{DG}} \geq 0.14$ ) in the central bulge volume (see Figures 3 and 4).

Observing HCN emission throughout the disk of the Milky Way is considerably more challenging given the required coverage and sensitivity. Helfer & Blitz (1997) constructed an unbiased, undersampled survey of HCN and CO emission along the Galactic plane between longitudes  $15^{\circ}5$  and  $55^{\circ}5$ , spaced by  $1^{\circ}$  intervals and  $b = 0^{\circ}$  with the NRAO 12 m telescope. Their HCN-to-CO ratio shows a flat profile with Galactic radius with an average value of 0.026 ( $f_{\text{DG}} = 0.06$ ). From this low value of  $R$  with respect to HCN/CO values observed toward resolved, active star-forming regions (0.1–0.3) within Galactic molecular clouds, they inferred that the HCN emission was originating from the more extended, lower-density ( $10^3 \text{ cm}^{-3}$ ) components of the clouds. Evans et al. (2020) imaged HCN  $J = 1 - 0$  emission from six molecular clouds in the first quadrant of the Milky Way. They determined HCN-to- $^{13}\text{CO}$  ratios between 0.04 and 0.12 but only a fraction (0%–57%) of the HCN luminosity comes from regions with  $A_v > 8$ , which is assumed to reflect high gas volume density where stars form. Battisti & Heyer (2014)

estimated the dense gas mass fraction for 344 clouds in the first quadrant of the Milky Way using ground-based thermal 1.1 mm dust continuum emission as a measure of dense gas mass and  $^{13}\text{CO } J = 1 - 0$  emission for the total cloud mass. While optically thin dust emission is a direct tracer of gas column density, data-processing methods used for ground-based millimeter continuum measurements to account for atmospheric contributions also remove extended emission from the larger clouds depending on the size of the cloud relative to the field of view of the bolometer array (Ginsburg et al. 2013). The resultant image identifies regions of overdensity within a cloud that typically correspond to dense clumps and filaments. Battisti & Heyer (2014) found  $f_{\text{DG}}$  values of 0.11 for all dust emission and 0.07 for subregions with mass surface densities greater than  $200 M_{\odot} \text{ pc}^{-2}$ , which likely represents higher volume densities. The fractions are found to be independent of cloud mass and mass surface density.

Figures 3 and 4 show  $f_{\text{DG}}$  values within the disk of M51 with a mean value of 0.05. This mean value is comparable to Milky Way values found by Helfer & Blitz (1997) and inferred from Evans et al. (2020) that point to a lower-density ( $\sim 10^3 \text{ cm}^{-3}$ ) origin where the HCN rotational energy levels are subthermally excited, resulting in weaker emission. The density of this component is still larger than the mean density of molecular clouds that is inferred from  $^{12}\text{CO}$  and  $^{13}\text{CO}$  emission.

## 6.2. $f_{\text{DG}}$ , Spiral Structure, and Stellar Bulge

A surprising result from our stacking analysis is the near-constant value of  $f_{\text{DG}} \sim 0.05$  between spiral-arm and interarm regions and throughout the disk component of M51. The actions of a spiral density wave are gas compression and



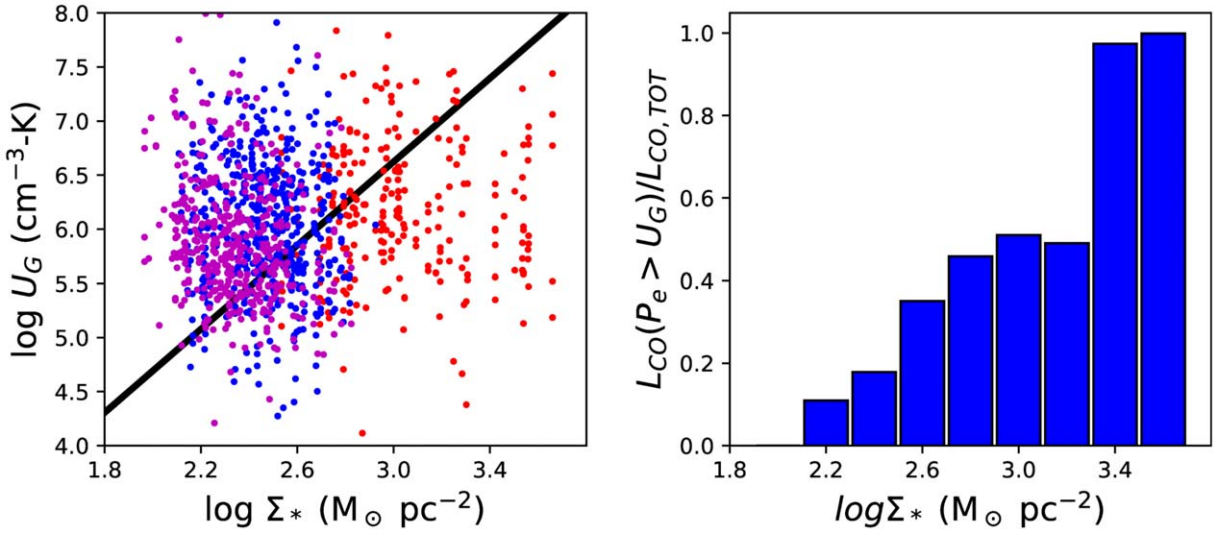


**Figure 7.** (Left) The self-gravitational energy densities for giant molecular clouds and cloud complexes in M51 within the central bulge region (red), spiral arms (blue), and interarm regions (magenta) from the compilation of molecular clouds in M51 by Colombo et al. (2014). The solid line shows the profile of kinematic pressure from the weight of the stars and molecular gas at the boundary of a cloud. Points below this line represent diffuse clouds. (Right) The fraction of CO luminosity from diffuse clouds for each  $\log \Sigma_*$  bin.

increased interstellar turbulence (Kim & Ostriker 2002) that contribute to the development of dense regions within molecular clouds. So, one might expect to find elevated values of  $f_{\text{DG}}$  in the spiral arms relative to those derived in the interarm regions.

The expected higher  $f_{\text{DG}}$  values in spiral arms can be resolved with our data if the conversion factor between CO luminosity and  $\text{H}_2$  mass is different in these respective domains. There is evidence that the CO conversion factor is  $\sim 2$  times larger in the interarm regions than in spiral arms in M51 and M83 (Wall et al. 2016). Adopting this arm–interarm dependence of the conversion factor would lead to  $f_{\text{DG}}$  values two times higher in the spiral arms than in the interarm regions.

Alternatively, the constant dense gas mass fraction throughout the disk could result from the density thresholds required to excite the HCN and CO lines within a population of stratified, self-gravitating clouds (Elmegreen 2018). For each spectral line, there is a unique cloud radius,  $r_c$ , at which the volume number density is equal to the line’s effective critical density,  $n_c$ . For a  $1/r^2$  density profile, the mass within this radius is proportional to  $r_c$ . Because  $r_c$  scales with  $n_c^{-1/2}$ , then the dense gas fraction derived from HCN and CO measurements is  $(n_{\text{CO}}/n_{\text{HCN}})^{1/2}$ , where  $n_{\text{CO}}$  and  $n_{\text{HCN}}$  are the critical densities for CO and HCN, respectively. For critical densities of  $100 \text{ cm}^{-3}$  for CO and  $10^4 \text{ cm}^{-3}$  for HCN,  $f_{\text{DG}} = 0.1$ , which is a reasonable estimate for the M51 values in the disk given the approximations of the effective critical densities described in Section 4.

Figure 4 shows the dense gas fraction begins to increase for  $\log(\Sigma_*) > 2.5$ . In this domain, the pressure,  $P_e$ , from the weight of stellar and gas components may exceed the gravitational energy density of a cloud,  $U_G = \frac{\pi G}{2} \Sigma_{\text{cloud}}^2$ , where  $\Sigma_{\text{cloud}}$  is the molecular gas surface density of an individual cloud. Clouds that satisfy the condition  $P_e > U_G$  are labeled as diffuse clouds (Elmegreen 2018). In Figure 7 we show the variation of  $U_G$  with  $\log(\Sigma_*)$  for giant molecular clouds and cloud complexes in M51 residing in the central region, spiral arms, and interarm regions from the catalog constructed by Colombo et al. (2014). The  $\Sigma_*$  value for each cloud is taken from the stellar-mass

surface density at the position of the cloud. The total midplane pressure can be approximated as

$$P_{\text{tot}} = \frac{\pi}{2} G \Sigma_{\text{gas}} \left( \Sigma_{\text{gas}} + \Sigma_* \frac{c_{g,\text{tot}}}{c_s} \right), \quad (7)$$

where  $c_s$  and  $c_{g,\text{tot}}$  are the star and gas velocity dispersions (Elmegreen 1989). At the cloud boundary, the kinematic pressure,  $P_e = P_{\text{tot}} / (1 + \alpha_o + \beta_o)$ , where  $\alpha_o = 0.46$  and  $\beta_o = 0.30$  are the relative cosmic-ray and magnetic field energy densities (Draine 2010). The measured gas velocity dispersion also requires a correction for cosmic rays and the interstellar magnetic field such that  $c_{g,\text{tot}} = c_g / (1 + \alpha_o + \beta_o)^{1/2}$ . From averages of  $\Sigma_{\text{mol}}$  and  $\Sigma_*$  over 1 kpc wide annular radii, we derive the relationship  $\Sigma_{\text{mol}} = 0.35 \Sigma_*^{0.95}$ . Assuming fully molecular gas ( $\Sigma_{\text{gas}} = \Sigma_{\text{mol}}$ ),  $c_s = 20 \text{ km s}^{-1}$  and  $c_g = 10 \text{ km s}^{-1}$ , we construct the profile of pressure with  $\Sigma_*$  from Equation (7). This profile of pressure with  $\log(\Sigma_*)$  is shown as the solid black line in Figure 7. For low values of  $\log(\Sigma_*)$  corresponding to the M51 disk (magenta and blue points), most clouds are above the pressure line, consistent with self-gravitating objects. In the central bulge, most of the defined objects (red points) lie below the pressure profile and are considered diffuse clouds.

From this information, the fraction of CO luminosity contributed by clouds with  $P_e > U_G$  for each  $\Sigma_*$  bin is calculated (see the right panel of Figure 7). For bins of stellar-mass surface densities greater than  $500 M_\odot \text{ pc}^{-2}$ ,  $>45\%$  of the molecular cloud mass resides within diffuse clouds. These fractions are also derived for the set of clouds in each region described by Colombo et al. (2014). The mass fraction of diffuse clouds is 91% in the central region, 14% in spiral arms, and 32% in the interarm regions.

The increasing fraction of molecular cloud mass in the diffuse state can account for the rise of the dense gas mass fraction at high stellar-mass surface densities. In the central 2 kpc, the neutral gas is already fully molecular (Jiménez-Donaire et al. 2019) so there is no available atomic hydrogen to

compress and contribute to the molecular mass. The external pressure can act upon the molecular gas to increase the mean density of the now diffuse molecular clouds. This compression leads to an increase in the dense gas mass fraction that is seen in Figures 3 and 4. At even higher stellar-mass surface densities within the central bulge, the pressure may even exceed the self-gravity energy density of the dense gas component. We note that for such conditions, our adopted value of  $\alpha_{\text{HCN}}$  is an upper limit (Gao & Solomon 2004b), which may increase  $\text{SFE}_{\text{dense}}$  values in the highest stellar-mass surface density bins and flatten the  $\text{SFE}_{\text{dense}}$  profile.

### 6.3. Environment and Star Formation Efficiency

The profiles of  $f_{\text{DG}}$  and the star formation efficiency with increasing stellar-mass surface density are clues for understanding the role of the galactic environment in the dynamical state of molecular clouds and the impact on the formation of new stars in galaxies. In M51, we find higher star formation efficiencies of dense gas in the disk, where the stellar-mass surface density and midplane pressure are low, and smaller values of  $\text{SFE}_{\text{dense}}$  in the central bulge, where  $\Sigma_*$  and pressures are high. Similar results have been established by earlier studies of M51 and other galaxies (Bigiel et al. 2016; Gallagher et al. 2018; Jiménez-Donaire et al. 2019). The transition between these regimes occurs between  $\log(\Sigma_*) \sim 2.5\text{--}3.0$ , where an increasingly larger fraction of the molecular mass resides within the diffuse cloud population (Figure 7).

Gallagher et al. (2018) and Jiménez-Donaire et al. (2019) propose that the lower dense gas star formation efficiencies in the high-pressure environment are a consequence of a higher mean density of clouds such that star formation occurs in regions of even higher volume densities than is traced by the HCN  $J=1-0$  line. The smaller volume and mass fraction of such overdense regions imply a larger amount of lower-density material that is contributing to the HCN  $J=1-0$  luminosity but is not actively forming stars, which leads to lower values of  $\text{SFE}_{\text{dense}}$ .

The proposed shift of star formation activity to higher-density regions can be understood if one considers the self-gravity of the dense protocluster clumps and protostellar cores as a fundamental requirement for the production of new stars. The formation of stars occurs when such structures collapse under their own self-gravity rather than implode from an external pressure disturbance. For high-pressure environments like the central bulge of M51, the condition  $U_G > P_e$  is realized at much higher surface and volume densities than are probed by the HCN  $J=1-0$  line.

A simple test for this description is to measure the variation of the star formation efficiency in dense gas using a tracer with a much higher critical density than the HCN  $J=1-0$  transition used in this and other studies. These data would directly trace the higher volume density and higher surface density regions that remain self-gravitating even under large external pressures. With a tracer of very high densities such that  $U_G > P_e$ , one would expect to see the  $\text{SFE}_{\text{dense}}$  profile to be flat or rising with increasing  $\Sigma_*$  and pressure.

## 7. Conclusions

Using  $^{12}\text{CO}$  and HCN  $J=1-0$  data with 582 pc resolution collected by the Large Millimeter Telescope and ancillary data from GALEX, Spitzer, SDSS, and 2MASS, we have investigated the variation of the dense gas mass fraction within different environments of the M51 galaxy and the impact on star formation. Within the disk component,  $f_{\text{DG}}$  can vary along a spiral-arm segment but on average, dense gas fractions are comparable in spiral arms and interarm regions. The dense gas mass fraction rises steeply in the central bulge, where the stellar-mass surface density is greater than  $500 M_{\odot}/\text{pc}^{-2}$ . The star formation efficiency of dense gas decreases with increasing stellar-mass surface density with an inflection point over  $\Sigma_* \sim 400\text{--}1000 M_{\odot} \text{pc}^{-2}$  that may mark a transition from self-gravitating structures to diffuse clouds and clumps. At the highest pressures in the central bulge, star formation is limited to more compact, high-density, self-gravitating structures that do not significantly contribute to the HCN  $J=1-0$  luminosity, which may lead to the measured decrease in the star formation efficiency of dense gas.

The authors thank the referee Frank Bigiel who provided valuable comments that improved the manuscript and LMT staff who helped with the observations. Support for the Large Millimeter Telescope is provided by NSF Grant AST-2034318 and Consejo Nacional de Ciencia y Tecnología (CONACYT) grants - U0004-246083, U0004-259839, F0003-272050, M0037-279006 and F0003-281692. Authors M.H., B.G., and D.C. acknowledge support from NSF grant AST-1907791. A.A. acknowledges the support of the Swedish Research Council, Vetenskapsrådet, and the Swedish National Space Agency (SNSA). This publication makes use of data products from the Two Micron All Sky Survey, which is a joint project of the University of Massachusetts and the Infrared Processing and Analysis Center/California Institute of Technology, funded by the National Aeronautics and Space Administration and the National Science Foundation. NASA/IPAC Extragalactic Database (NED) is funded by the National Aeronautics and Space Administration and operated by the California Institute of Technology.

*Facility:* LMT(SEQUOIA).

*Software:* astropy (Astropy Collaboration et al. 2013), emcee (Foreman-Mackey et al. 2013), bces (Nemmen et al. 2012).

## Appendix Galfit Model Parameters

To estimate the contributions from the old stellar population, we decompose the Spitzer 3.6  $\mu\text{m}$  image of surface brightness into model components using Galfit (Peng et al. 2010). The parameters for each model component are described in Peng et al. (2010). The values of the best-fit parameters derived for M51 for SFR Model 1 and SFR Model 2 are listed in Tables 4 and 5. Figure 8 shows the superpositions of all model components that are fit to the Spitzer 3.6  $\mu\text{m}$  intensities and from which the cirrus contributions are estimated for SFR Model 1 and Model 2.

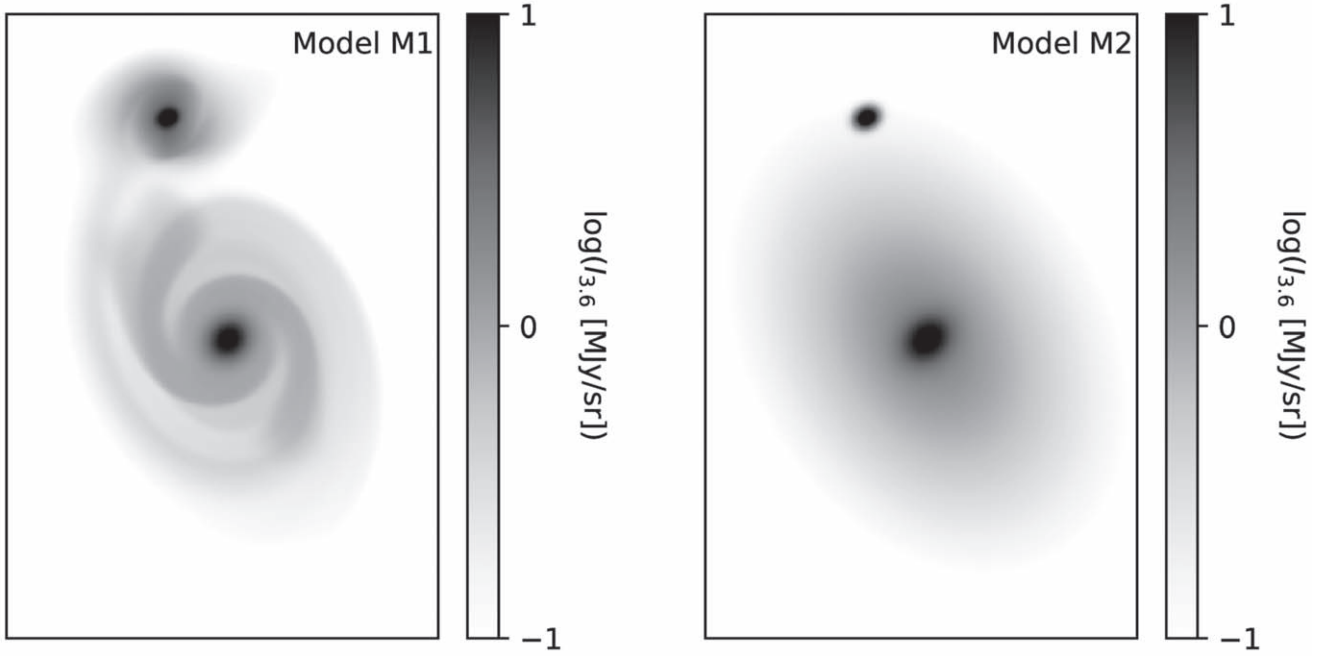


**Figure 8.** Galfit models of 3.6  $\mu\text{m}$  surface brightness for (left) Model 1 with bulge and spiral-arm components and (right) Model 2 with bulge component and an exponential disk with no spiral arms.


**Table 4**  
Galfit Parameters for Model 1

Parameter	#	Sérsic Power Fourier	$\delta x$ (") ... $a_1$	$\delta y$ (") $r_{in}(')$ $\phi_1$ (deg)	mag $r_{out}(')$ $a_3$	$r_e(')$ $\theta_{rot}$ (deg) $\phi_3$ (deg)	$n$ $\alpha$ $a_4$	$q$ $\theta_{incl}$ (deg) $\phi_4$ (deg)	$\theta_{P.A.}$ (deg) $\theta_{sky}$ (deg) $a_5$	$\phi_5$ (deg)	Comment
M51a	1	Sérsic	-0.09	-0.18	13.0	0.040	1.18	0	-65.5		bulge
	2	Sérsic	0.17	0.31	10.3	0.260	0.67	0	-47		bulge
	3	Sérsic power	3.4 -1.29	2.0 -1.29	8.9 4.28	2.780 -791	0.35 0.29	0 40	-26 -74		outer spiral
	4	Fourier Sérsic power	-0.117 -3.3 0.66	55.3 0.8 0.66	-0.006 10.0 2.34	-18.9 1.88 -194	0.041 0.14 -0.11	-33.7 0 -0.01	0.023 19 29	28.2	inner spiral
M51b	5	Fourier Sérsic	-0.122 -69.7	11.4 255.4	-0.056 11.9	-55.5 0.0428	0.058 0.38	3.9 0	0.014 -82	4.1	bulge
	6	Sérsic	-69.4	255.5	11.0	0.1107	0.74	0	-64		bulge
	7	Sérsic	-72.1	252.4	9.9	0.900	0.72	0	-25		spiral
		power Fourier	0.880 -0.128	1.08 113.4	1.08 -0.070	32 -1.0	1.6 0.020	42 18.6	49 0.018	8.3	

**Table 5**  
Galfit Parameters for Model 2

Parameter	#	Sérsic Power Fourier	$\delta x$ (") ... $a_1$	$\delta y$ (") $r_{in}(')$ $\phi_1$ (deg)	mag $r_{out}(')$ $a_3$	$r_e(')$ $\theta_{rot}$ (deg) $\phi_3$ (deg)	$n$ $\alpha$ $a_4$	$q$ $\theta_{incl}$ (deg) $\phi_4$ (deg)	$\theta_{P.A.}$ (deg) $\theta_{sky}$ (deg) $a_5$	$\phi_5$ (deg)	Comment
M51a	1	Sérsic	-0.08	-0.17	13.1	0.0340	0.92	0	-82		bulge
	2	Sérsic	0.17	0.29	9.9	0.3200	0.76	0	-51		bulge
	3	Sérsic	0.17	0.29	8.0	2.4	0.82	0	31		disk
M51b	4	Sérsic	-69.6	255.4	11.6	0.04	0.38	0	-81		bulge
	5	Sérsic	-69.5	255.4	10.9	0.113	0.75	0	-63		bulge
	6	Sérsic	-68.7	259.3	9.6	0.96	0.70	0	-26		spiral
		power Fourier	0.927 0.060	1.38 96.3	1.38 0.023	39 -57.0	1.7 0.056	50 20.5	51 0.016	10.6	

## ORCID iDs

Mark Heyer  <https://orcid.org/0000-0002-3871-010X>  
 Benjamin Gregg  <https://orcid.org/0000-0003-4910-8939>  
 Daniela Calzetti  <https://orcid.org/0000-0002-5189-8004>  
 Bruce G. Elmegreen  <https://orcid.org/0000-0002-1723-6330>  
 Robert Kennicutt  <https://orcid.org/0000-0001-5448-1821>  
 Angela Adamo  <https://orcid.org/0000-0002-8192-8091>  
 Aaron S. Evans  <https://orcid.org/0000-0003-2638-1334>  
 Kathryn Grasha  <https://orcid.org/0000-0002-3247-5321>  
 James D. Lowenthal  <https://orcid.org/0000-0001-9969-3115>  
 Gopal Narayanan  <https://orcid.org/0000-0002-4723-6569>  
 Daniel Rosa-Gonzalez  <https://orcid.org/0000-0003-1327-0838>  
 F. P. Schloerb  <https://orcid.org/0000-0002-2726-9443>  
 Kamal Souccar  <https://orcid.org/0000-0001-7915-5272>  
 Peter Teuben  <https://orcid.org/0000-0003-1774-3436>  
 Olga Vega  <https://orcid.org/0000-0002-2852-9737>  
 William F. Wall  <https://orcid.org/0000-0001-6142-397X>  
 Min S. Yun  <https://orcid.org/0000-0001-7095-7543>

## References

- Aihara, H., Allende Prieto, C., An, D., et al. 2011, *ApJS*, 193, 29  
 Akritas, M. G., & Bershady, M. A. 1996, *ApJ*, 470, 706  
 André, P., Di Francesco, J., Ward-Thompson, D., et al. 2014, in *Protostars and Planets VI*, ed. H. Beuther et al. (Tucson, AZ: Univ. Arizona Press), 27  
 Aniano, G., Draine, B. T., Gordon, K. D., & Sandstrom, K. 2011, *PASP*, 123, 1218  
 Astropy Collaboration, Robitaille, T. P., Tollerud, E. J., et al. 2013, *A&A*, 558, A33  
 Barnes, A. T., Longmore, S. N., Battersby, C., et al. 2017, *MNRAS*, 469, 2263  
 Battisti, A. J., & Heyer, M. H. 2014, *ApJ*, 780, 173  
 Bergin, E. A., & Tafalla, M. 2007, *ARA&A*, 45, 339  
 Beuther, H., Leurini, S., Schilke, P., et al. 2007, *A&A*, 466, 1065  
 Bigiel, F., Leroy, A., Walter, F., et al. 2008, *AJ*, 136, 2846  
 Bigiel, F., Leroy, A. K., Jiménez-Donaire, M. J., et al. 2016, *ApJL*, 822, L26  
 Bolatto, A. D., Wolfire, M., & Leroy, A. K. 2013, *ARA&A*, 51, 207  
 Brown, M. J. I., Moustakas, J., Smith, J. D. T., et al. 2014, *ApJS*, 212, 18  
 Bruzual, G., & Charlot, S. 2003, *MNRAS*, 344, 1000  
 Chen, H., Gao, Y., Braine, J., & Gu, Q. 2015, *ApJ*, 810, 140  
 Colombo, D., Hughes, A., Schinnerer, E., et al. 2014, *ApJ*, 784, 3  
 Dame, T. M. 2011, arXiv:1101.1499  
 de los Reyes, M. A. C., & Kennicutt, R. C. J. 2019, *ApJ*, 872, 16  
 Dobbs, C. L., Theis, C., Pringle, J. E., & Bate, M. R. 2010, *MNRAS*, 403, 625  
 Draine, B. 2010, *Physics of the Interstellar and Intergalactic Medium*, Princeton Series in Astrophysics (Princeton, NJ: Princeton Univ. Press)  
 Elmegreen, B. G. 1989, *ApJ*, 338, 178  
 Elmegreen, B. G. 1993, *ApJ*, 411, 170  
 Elmegreen, B. G. 2018, *ApJ*, 854, 16  
 Evans, N. J. I., Kim, K.-T., Wu, J., et al. 2020, *ApJ*, 894, 103  
 Foreman-Mackey, D., Hogg, D. W., Lang, D., & Goodman, J. 2013, *PASP*, 125, 306  
 Gallagher, M. J., Leroy, A. K., Bigiel, F., et al. 2018, *ApJ*, 858, 90  
 Gao, Y., & Solomon, P. M. 2004a, *ApJ*, 606, 271  
 Gao, Y., & Solomon, P. M. 2004b, *ApJS*, 152, 63  
 Gieser, C., Beuther, H., Semenov, D., et al. 2021, *A&A*, 648, A66  
 Gil de Paz, A., Boissier, S., Madore, B. F., et al. 2007, *ApJS*, 173, 185  
 Ginsburg, A., Glenn, J., Rosolowsky, E., et al. 2013, *ApJS*, 208, 14  
 Goicoechea, J. R., Lique, F., & Santa-Maria, M. G. 2022, *A&A*, 658, A28  
 Goldsmith, P. F., & Kauffmann, J. 2017, *ApJ*, 841, 25  
 Helfer, T. T., & Blitz, L. 1997, *ApJ*, 478, 233  
 Jackson, J. M., Heyer, M. H., Paglione, T. A. D., & Bolatto, A. D. 1996, *ApJL*, 456, L91  
 Jarrett, T. H., Chester, T., Cutri, R., Schneider, S. E., & Huchra, J. P. 2003, *AJ*, 125, 525  
 Jiménez-Donaire, M. J., Bigiel, F., Leroy, A. K., et al. 2019, *ApJ*, 880, 127  
 Jones, P. A., Burton, M. G., Cunningham, M. R., et al. 2012, *MNRAS*, 419, 2961  
 Kennicutt, R. C. J. 1989, *ApJ*, 344, 685  
 Kennicutt, R. C. J. 1998, *ApJ*, 498, 541  
 Kennicutt, R. C. J., & Armus, L. 2003, *PASP*, 115, 928  
 Kennicutt, R. C. J., Calzetti, J., Walter, D., et al. 2007, *ApJ*, 671, 333  
 Kennicutt, R. C., & Evans, N. J. 2012, *ARA&A*, 50, 531  
 Kim, W.-T., & Ostriker, E. C. 2002, *ApJ*, 570, 132  
 Koda, J., Scoville, N., Sawada, T., et al. 2009, *ApJL*, 700, L132  
 Koda, J., Sawada, T., Wright, M. C. H., et al. 2011, *ApJS*, 193, 19  
 Kreckel, K., Blanc, G. A., Schinnerer, E., et al. 2016, *ApJ*, 827, 103  
 Kroupa, P. 2001, *MNRAS*, 322, 231  
 Kruijssen, J. M. D., Longmore, S. N., Elmegreen, B. G., et al. 2014, *MNRAS*, 440, 3370  
 Krumholz, M. R., Dekel, A., & McKee, C. F. 2012, *ApJ*, 745, 69  
 Leroy, A. K., Walter, F., Brinks, E., et al. 2008, *AJ*, 136, 2782  
 Leroy, A. K., Bigiel, F., de Blok, W. J. G., et al. 2012, *AJ*, 144, 3  
 Leroy, A. K., Schinnerer, E., Hughes, A., et al. 2017, *ApJ*, 846, 71  
 Liu, G., Koda, J., Calzetti, D., Fukuhara, M., & Momose, R. 2011, *ApJ*, 735, 63  
 Longmore, S. N., Bally, J., Testi, L., et al. 2013, *MNRAS*, 429, 987  
 Lu, X., Mills, E. A. C., Ginsburg, A., et al. 2019, *ApJS*, 244, 35  
 McQuinn, K. B. W., Skillman, E. D., Dolphin, A. E., Berg, D., & Kennicutt, R. 2016, *ApJ*, 826, 21  
 Meidt, S. E. 2016, *ApJ*, 818, 69  
 Meidt, S. E., Schinnerer, E., Knapen, J. H., et al. 2012, *ApJ*, 744, 17  
 Myers, P. C., & Benson, P. J. 1983, *ApJ*, 266, 309  
 Narayanan, G., Heyer, M. H., Brunt, C., et al. 2008, *ApJS*, 177, 341  
 Nemmen, R. S., Georganopoulos, M., Guiriec, S., et al. 2012, *Sci*, 338, 1445  
 Paglione, T. A. D., Jackson, J. M., Bolatto, A. D., & Heyer, M. H. 1998, *ApJ*, 493, 680  
 Peng, C. Y., Ho, L. C., Impney, C. D., & Rix, H.-W. 2010, *AJ*, 139, 2097  
 Pety, J., Schinnerer, E., Leroy, A. K., et al. 2013, *ApJ*, 779, 43  
 Pokhrel, R., Gutermuth, R. A., Krumholz, M. R., et al. 2021, *ApJL*, 912, L19  
 Querejeta, M., Meidt, S. E., Schinnerer, E., et al. 2015, *ApJS*, 219, 5  
 Querejeta, M., Schinnerer, E., Schrubba, A., et al. 2019, *A&A*, 625, A19  
 Rahman, N., Bolatto, A. D., Wong, T., et al. 2011, *ApJ*, 730, 72  
 Schinnerer, E., Meidt, S. E., Pety, J., et al. 2013, *ApJ*, 779, 42  
 Schlafly, E. F., & Finkbeiner, D. P. 2011, *ApJ*, 737, 103  
 Schmidt, M. 1959, *ApJ*, 129, 243  
 Shetty, R., Kelly, B. C., & Bigiel, F. 2013, *MNRAS*, 430, 288  
 Shirley, Y. L. 2015, *PASP*, 127, 299  
 Wall, W. F., Puerari, I., Tilanus, R., et al. 2016, *MNRAS*, 459, 1440  
 Willmer, C. N. A. 2018, *ApJS*, 236, 47  
 Wu, J., Evans, N. J. I., Shirley, Y. L., & Knez, C. 2010, *ApJS*, 188, 313  
 Zibetti, S. 2009, arXiv:0911.4956  
 Zibetti, S., Charlot, S., & Rix, H.-W. 2009, *MNRAS*, 400, 1181